J. Phys. B: At. Mol. Opt. Phys. **42** (2009) 025402 (9pp) doi:10.1088/0953-4075/42/2/025402

Resonant scattering states in 2D nanostructured waveguides: a boundary wall approach

F M Zanetti[1,2], M L Lyra[2], F A B F de Moura[2] and M G E da Luz[1]

[1] Departamento de Física, Universidade Federal do Paraná, 81531-990 Curitiba PR, Brazil
[2] Departamento de Física, Universidade Federal de Alagoas, 57072-970 Maceió AL, Brazil

E-mail: luz@fisica.ufpr.br

Received 7 August 2008, in final form 28 November 2008
Published 29 December 2008
Online at stacks.iop.org/JPhysB/42/025402

Abstract
We determine resonant scattering states of two-dimensional photonic crystal nanostructures with defects. To do so, we use the boundary-wall method originally introduced to obtain the scattering eigenstates of one electron moving in a medium with arbitrary boundaries. We investigate geometries including beam bending and interferometer-like waveguides, as well as waveguides connected by resonant cavities. We are able to identify the electromagnetic modes that, due to the special resonance condition attained in the vicinity of defects, provide optimal transmission of an incoming plane wave. Based on the generality of the boundary wall technique and its numerical simplicity and efficiency to identify resonant scattering modes, we briefly discuss further possible applications of this method in analysing the performance of general photonic band-gap devices.

1. Introduction

The close analogy between quantum electronic transport in crystals and electromagnetic wave propagation in dielectric media has been explored since the early age of quantum mechanics. One of the most striking examples is the tunnelling effect, where an electron may overcome a classically forbidden potential barrier, a phenomenon formally equivalent to the partial transmission of electromagnetic waves through a dielectric slab. As recent developments in optical communication systems have overcome electron-based technology, in both speed and bandwidth, there has been a growing movement towards the study of new dielectric media, commonly termed *photonic crystals* [1–3]. These systems are composed of periodic optical media whose manipulation can tailor light propagation in the same way as electronic transport is controlled in different device structures.

Among the wealth of research work on photonic crystals, the study of dielectric structures at which the optical band displays a photonic band gap is of particular interest [4]. In these structures, there is a frequency range for which light propagation is forbidden. The picture is quite similar to that of a semiconductor. One of the main motivations to study such systems lies in the use of photonic band gaps to inhibit spontaneous emission of light [5]. Further, defects in a semiconductor structure induce the emergence of localized electronic states, whose positions within the energy band can be tuned. The transistor electronics enabled by this effect have promoted the huge technological revolution of the last half-century. Thus, the creation of localized light states by means of intentional defects in photonic crystals points towards the possibility of optical devices mimicking all the features of electronic devices. The advantage is the fact that the present technology permits almost unlimited control over the size and shape of defects on the typical optical length scale.

Besides the technical advantages of photonic crystal devices over traditional electronic ones, there is a physical property of photons which makes the theoretical studies based on the photonic band structure more reliable than their equivalent for electrons: photons are essentially non-interacting. Hence, band-structure calculations of photonic crystals can be considered a very precise description while it is usually just a first approximation for electrons (once the Coulomb interaction plays a decisive role in many relevant situations [6]). Much of the theoretical effort devised to study photonic crystals has been devoted to the extension of mathematical and computational methods of solid-state

physics to obtain band diagrams, transmission spectra and optical scattering eigenmodes.

In this work we depart from the standard numerical approaches to studying photonic crystals. We consider the so-called boundary wall method (BWM) [7], a scattering-based technique which clearly contrasts with those already existing for photonic crystals (see, e.g., [8]). Originally, it was developed to analyse scattering by wall potentials in quantum mechanics and used, for instance, to calculate the conductance of quantum point contacts coupled to open resonators [9] and matter waves in quantum wires and atomic arrays [10]. We show that such a method can be used successfully to obtain the resonant scattering modes of nanostructured photonic crystal waveguides with defects. The BWM presents many interesting features, such as the ability to deal with disconnected and open boundaries, being numerically simple and computationally fast.

We will be particularly interested in identifying the resonant modes of 2D photonic band gap structures with defects composed of a square lattice arrangement of nanosized rods. These photonic structures support the transmission of beam bending localized states, interferometric phenomena, as well as wave guiding mediated by resonant cavities.

This paper is organized as follows. In the following section we describe the main ideas behind the method and how to extend it to the problem of scattering states of Maxwell's equations for dielectric materials. In section 3 we apply the BWM to beam bending and interferometer-like waveguide geometries. The case of resonant cavities is addressed in section 4. Finally, in section 5 we summarize and briefly discuss further potential applications of the boundary wall method.

2. The boundary wall method

A few years ago, a new approach, the boundary wall method (BWM) [7], was developed to solve the problem of a particle scattered off by arbitrary disconnected open or closed sharp-walled boundaries such as billiards, waveguides and various compound objects, e.g., baffles, chambers, etc. It allows us to impose penetrable, Dirichlet, Neumann and mixed boundary conditions along the scatters walls. The original derivations were focused on the Schrödinger equation in two dimensions. Nevertheless, the method can easily be extended to other wave equations in two or more spatial dimensions.

In this section we give a brief summary of the BWM, also discussing how it can be used to calculate electromagnetic fields in photonic crystal structures. A full account of the BWM can be found in the original work [7], as well as in a very recent technical review [11].

2.1. The BWM formulation

Consider scatters of arbitrary shape $\mathcal{C}$, presenting *penetrable or leaky boundary conditions*. Now, for the 'δ-wall' potential $V(\mathbf{r}) = \int_{\mathcal{C}} \mathrm{d}s\gamma(s)\delta(\mathbf{r} - \mathbf{r}(s))$, one finds from the Lippmann–Schwinger equation that the wavefunction of energy $E = k^2$ is given by

$$\Psi(\mathbf{r}) = \varphi(\mathbf{r}; k) + \int_{\mathcal{C}} \mathrm{d}s\, \gamma(s) G_0(\mathbf{r}, \mathbf{r}(s); k)\Psi(\mathbf{r}(s)). \quad (1)$$

In the above, the integration is over $\mathcal{C}$, the connected or disconnected boundary, with $\mathbf{r}(s)$ the vector position of a point s on $\mathcal{C}$. $\varphi(\mathbf{r}; k)$ solves $(\nabla^2 + k^2)\varphi(\mathbf{r}; k) = 0$ in the whole plane and the free Green function satisfies $(\nabla^2 + k^2)G_0(\mathbf{r}, \mathbf{r}_0; k) = \delta(\mathbf{r} - \mathbf{r}_0)$, which in 2D results in $G_0(\mathbf{r}, \mathbf{r}_0; k) = (4i)^{-1} H_0^{(+)}(k|\mathbf{r}-\mathbf{r}_0|)$, with $H_0^{(+)}$ the zero-order Hankel function of the first kind.

We can interpret $\mathcal{C}$ as a leaky wall characterized by the permeability parameter $\gamma(s)$. As proved in details in [7], any plane wave of wavenumber k, incident perpendicular to the point s on $\mathcal{C}$, has the probability $4k^2/(4k^2 + \gamma(s)^2)$ to be transmitted through and $\gamma(s)^2/(4k^2 + \gamma(s)^2)$ to be reflected from s. If for any s we take the limit $\gamma(s) \to \infty$, the probability of transmission goes to zero. This is equivalent to a vanishing wave on $\mathcal{C}$, thus leading to the usual Dirichlet impenetrable boundary condition [7, 11]. The Neumann and mixing boundary conditions can be implemented by a direct extension of the method [7].

To solve equation (1), we write the relation between the incident wave $\varphi(\mathbf{r}_a)$ and the scattered $\Psi(\mathbf{r}_b)$, with $\mathbf{r}(s_a) = \mathbf{r}_a$ and $\mathbf{r}(s_b) = \mathbf{r}_b$ vector positions of arbitrary points s_a and s_b on $\mathcal{C}$, as

$$\Psi(\mathbf{r}_b) = \int_{\mathcal{C}} \mathrm{d}s_a\, T_\gamma(s_b, s_a; k)\varphi(\mathbf{r}_a). \quad (2)$$

Then, in order to satisfy equation (1), T_γ must obey

$$T_\gamma(s_b, s_a; k) = \delta(s_b - s_a) + \int_{\mathcal{C}} \mathrm{d}s\, G_0(\mathbf{r}_b, \mathbf{r}(s); k) \times \gamma(s) T_\gamma(s, s_a; k). \quad (3)$$

Finally, using relation (2) in (1), we arrive at the solution for the scattered wave, or

$$\Psi(\mathbf{r}) = \varphi(\mathbf{r}) + \int_{\mathcal{C}}\int_{\mathcal{C}} \mathrm{d}s_b\, \mathrm{d}s_a G_0(\mathbf{r}, \mathbf{r}_b; k) \times \gamma(s_b) T_\gamma(s_b, s_a; k)\varphi(\mathbf{r}_a; k). \quad (4)$$

Here we have reached the method's central idea. If somehow T_γ can be obtained (e.g., directly from its definition, equation (3), or from a numerical implementation, see below), then the wavefunction everywhere is calculated by simple quadratures over $\mathcal{C}$.

At this point, the main difference between the BWM and other Green function methods (GFM) [12] becomes clear. In general, the use of GFM leads to the scattered fields through N integral equations (with N the number of lattice scatterers), involving the field, the Green function and their normal derivatives at the media interfaces. Also, different sets of equations are necessary for each domain (inside/outside). The resulting equations can be solved numerically by various procedures, a common one being the boundary integral method [13]. In the BWM, the scattering states for all space (both inside and outside the scatterers) are obtained from the integration of equation (4), which encompass only the known quantities $G_0(\mathbf{r}, \mathbf{r}(s))$, $\gamma(s)$ and T_γ (this latter being

a function of G_0 and γ over $\mathcal{C}$, equation (3)). Using the BWM for photonic crystals, all the rods are faced as a unique, although disconnected, boundary. So, equation (4) describes the full scattering process at once, in contrast to some multiple-scattering or recursive treatments [14, 15].

The particular case of infinite γ is easily handled through a simple mathematical trick [7]. It is relevant when the Dirichlet impenetrable boundary conditions [16] are applied to photonic crystal lattices. In fact, for many purposes, e.g., to minimize the losses in the substrate or to increase the band gap, one must increase the dielectric contrast difference between the substrate and the crystal structure [17]. Thus, in the ideal situation the refraction index of the latter should go to infinity, as in metallic materials [18], for which the BWM with $\gamma \to \infty$ has already been used to demonstrate negative refraction features of microwave photonic crystals [19].

From a practical point of view, in general it is difficult to obtain exact analytical formulae for T and thus for Ψ (a few examples are given in [7, 11]). Nevertheless, different numerical ways to implement the BWM for a complete arbitrary boundary $\mathcal{C}$ are discussed in [7] and also in [9, 10]. Furthermore, a very simple and efficient numerical protocol—based on the discretization of the equation (1) and on the derivation of an algebraic expression for a finite matrix version of T in equation (2)—is presented in [11] and outlined in the appendix. This is the approach we are going to use next in all our applications.

2.2. Relation with Maxwell's solution

There is a very profound formal similarity between quantum-mechanical particles propagating in periodic 3D media and the solution of free Maxwell's equations for electromagnetic waves. For instance, for a fixed frequency ω, one can write independent equations for the magnetic field $\mathbf{H}$ and electric field $\mathbf{E}$ as eigenvalue problems with Hermitian operators. Hence, in many aspects they resemble the Schrödinger equation (see, e.g., the discussion in [2]). This similarity is even stronger if the relevant dynamics is restricted to two dimensions. Indeed, by considering a structure as shown in figure 1, where all the rods have the same constant permeability γ, the electromagnetic wave problem reduces to solving a Helmholtz equation in 2D, for either the electric or magnetic fields [20, 21], corresponding to TE and TM modes. The fields are subjected to the appropriate penetrable boundary conditions along the photonic crystal, i.e., at the scatter $\mathcal{C}$, formed by the collection of rods (which in real systems are filled with the dielectric material but here represented only by dielectric shells). So, by using the BWM, one should solve equation (4) by identifying the function Ψ with, say, the electric field (TE mode) along the photonic crystal cavities, and associating $k^2 = \varepsilon\mu\omega^2/c^2$, where ε is the substrate dielectric constant and μ is the magnetic permeability.

The permeability γ of the scatterers can be related to the dielectric constant by considering the transmission coefficient $\mathcal{T}$ in terms of the field square. For an electric field $\mathbf{E}(\mathbf{r})$ incident normally to the interface between two (non-magnetic $\mu = \mu_0$) dielectric media of refraction indexes n_1 and n_2, we have

$$\mathcal{T}_{\mathrm{EM}} = \frac{|\mathbf{E}_2(\mathbf{r}(s))|^2}{|\mathbf{E}_1(\mathbf{r}(s))|^2} = \frac{4n_1^2}{(n_1+n_2)^2}. \tag{5}$$

As mentioned before, the relation between the normal transmission through some point s in the boundary of a scatterer and its permeability γ is given by (for derivations, we invite the reader to refer to [7])

$$\mathcal{T} = \frac{4k^2}{4k^2+\gamma(s)^2}. \tag{6}$$

Qualitatively, the above expression is very simple to understand. Indeed, thinking in terms of a plane wave incident perpendicular to $\mathcal{C}$ at s, along such a direction the boundary acts like an effective 1D δ-function potential, thus splitting the wave into reflected and transmitted parts at s accordingly. Equation (6) is exactly the δ-function transmission probability for the case of a wavenumber k.

Using the relative index between the media ($n_2/n_1 = n_r$) and making $\mathcal{T}_{\mathrm{EM}}$ equal to $\mathcal{T}$, we have for γ

$$\gamma = k\sqrt{(n_r+1)^2-4}, \tag{7}$$

which yields the value of the permeability γ of a boundary as a function of its index of refraction n_r.

3. Applications I: beam bending and interferometer-like waveguides

In the present and following section we discuss 2D photonic crystal structures, whose defects are of air-type, i.e., those where scatterers are completely removed from the lattice. For the ratio between the lattice constant a_0 and the scatterer radius r we take $a_0/r = 5$, where any spatial dimension is given in arbitrary units. As the refraction index of the scattering rods we set $n = 3.4$ (typical of GaAs in the infrared regime). For the incident field, we always consider plane waves along the x direction, i.e., $\varphi(\mathbf{r}; k) = \exp[ikx]$. Finally, the size of the T matrix used in all simulations is such that each rod is discretized in ten segments Δs (see the appendix), which yields $\lambda/\Delta s \approx 22$ for the minor wavelength used.

We start with a $\pi/2$ line-defected waveguide in a finite photonic crystal (see, e.g., [2, 22]). The exact geometry and spatial dimensions are depicted in figure 1. We shall study transmission along the waveguide. Since the initial plane-wave field comes from the left, we have added to the structure an impenetrable wall ($\gamma \to \infty, n \to \infty$) as shown in figure 1. Such a procedure is useful in the forthcoming analysis, once it guarantees that any appreciable amplitude for the field at the waveguide vertical arm's end can result only from a resonant transmission. For better visualization, hereafter all the plots are normalized so that the overall highest amplitude in each figure is equal to 1.

We have investigated the scattering states for many different values of kr. Here we show only two representative examples, namely, $kr = 0.459$ and $kr = 0.27$, whose corresponding wavelengths $\lambda = 2\pi/k$ are schematically represented in figure 1. In figure 2 we plot a 2D density plot of $|\Psi|^2$ for $kr = 0.27$. We see that within the photonic crystal the

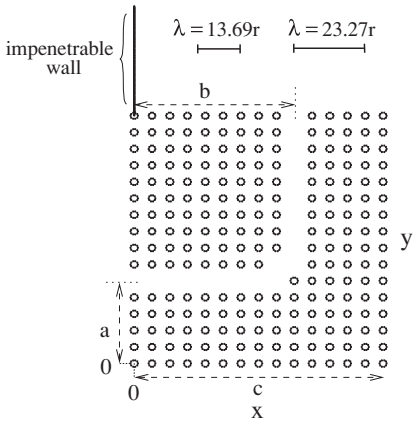

Figure 1. Schematics of the $\pi/2$ line-defect waveguide in a finite photonic crystal-like system constituted of penetrable rods of radius r and lattice spacing $a_0 = 5r$. The other distances are $a = 5a_0$, $b = 9a_0$ and $c = 14a_0$. The wavelengths corresponding to $kr = 0.459$ and $kr = 0.27$ are also shown for comparison. The origin of the x–y plane is at the centre of the farther bottom-left rod.

field is practically null. Also, the intensity is vanishingly small along the waveguide, as verified from the one-dimensional 'cuts' of $|\Psi|^2$ crossing the line-defect arms. In the region surrounding the finite lattice, we observe the expected steady wave scattering pattern.

Figure 3 displays the case of $kr = 0.459$, for which resonant transmission takes place. Our result is consistent with a previous study [22] of a similar structure (with a slightly larger aspect ratio, $kr = 0.40$ and $a_0/r = 5.55$), where a sophisticated vector finite-difference time-domain algorithm with quartic perfectly matched layer boundaries has been used to characterize the transmission features. In figure 3 the observed crescent profile of the beam along the vertical arm (best visualized in the 3D plot), a kind of 'candle flame' effect, is due to the vanishing of the backscattering effect as the end of the waveguide approaches. Note also that within the photonic crystal $|\Psi|^2$ vanishes. This resonant mode of wavelength $\lambda = 13.69r$ can be tuned from the visible light to the near-infrared spectrum (400 nm $< \lambda <$ 1400 nm) varying the radius of the scatterers in the range between 30 and 100 nm. Additional tuning can be performed by adjusting the aspect ratio a_0/r and the scatterers refraction index.

Next, we consider the interferometer-like waveguide, schematically represented in figure 4. It consists of lower and upper arms (starting at $x = 0$), which are connected to each other by a perpendicular line defect. A middle arm leaves from the latter, ending at $x = c$. We investigate the field profiles inside the waveguide. As examples, we take $kr = 0.333$ and $kr = 0.459$, whose corresponding wavelengths are represented in figure 4. We show in figures 5 and 6 the resulting density plots. In each case, we also display cuts of $|\Psi|^2$ crossing the lower and middle arms. Due to the symmetry, the field in the lower and upper arms is exactly the same, as we have checked numerically.

For $kr = 0.333$ (figure 5), the square of the field has its maximum at the 'entrances' of the two left arms, decaying to around 37% of this value at their ends in $x = b$. Along the middle and perpendicular arms, the field is low but not null, with peaks for $|\Psi|^2$ of about 10% of the overall maximum value. On the other hand, in figure 6 we see a perfect constructive interference for $kr = 0.459$. The perpendicular and parallel arms present identical structures of maxima and minima for $|\Psi|^2$. It favours the resonant transmission at the middle arm, where the square of the field reaches in the arm's end region a value very close to its possible maximum intensity. Here again we observe the 'candle flame' effect.

Finally, by changing the waveguide arms size we test how different optical path lengths influence the field inside the structure. The results for $kr = 0.459$ are displayed in figure 7, where we show 2D density plots of $|\Psi|^2$ for three different situations, namely, the bottom leg of the perpendicular arm

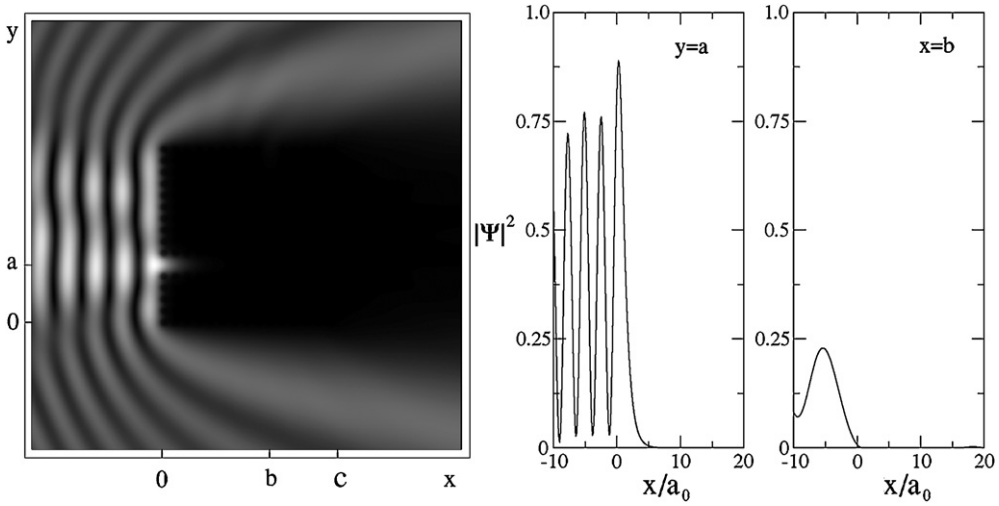

Figure 2. A 2D density plot of $|\Psi|^2$ for the incident plane wave $\varphi(\mathbf{r}) = \exp[ikx]$, with $kr = 0.27$. Darker regions correspond to lower intensities. It is also shown 'cuts' of $|\Psi|^2$ along $y = a$ and $x = b$, therefore crossing the waveguide arms. For better visualization the results are normalized so that the overall highest amplitude is equal to 1.

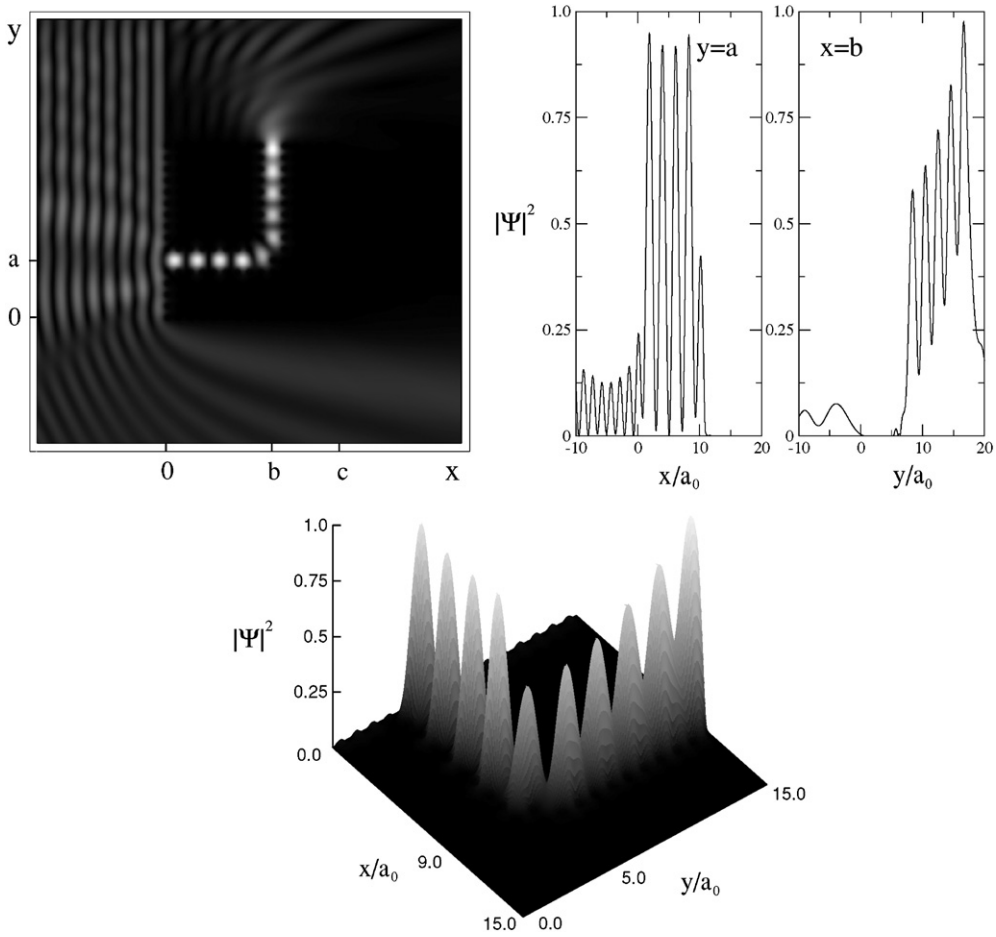

Figure 3. Same as figure 2, but for $kr = 0.459$. Here a resonance transmission along the waveguide is clearly seen. The bottom 3D plot shows a more detailed view of $|\Psi|^2$ within the photonic crystal region. Outside the line-defected waveguide the field is practically null.

is one, two or three row of rods longer than the top leg. We clearly see that different spatial configurations of the line defects lead to different patterns for the field within the waveguide. An outgoing light beam can be produced once the resonance condition for beam bending is satisfied and the optical path length difference favours constructive interference. We should stress that a Mach–Zehnder photonic crystal based interferometer has recently been proposed in the literature [23].

4. Applications II: resonant cavity and cavity coupled to waveguides

In analogy with impurity in semiconductors, the introduction of certain kinds of defects in the periodic crystal lattice can create an eigenstate associated with it, with energy belonging to the band gap of the periodic structure [1]. As in the waveguide case, the suppression of transmission between the rods makes the structure work as a reflective wall, forming a resonant cavity at which the mode becomes trapped [2]. The kind of defect that yields such modes is of point-type. It can be produced, for example, by varying the radius or index of refraction of some of the scatterers [3].

In figure 8 we show the numerical results for a lattice with a cavity produced by the removal of the central scatterer

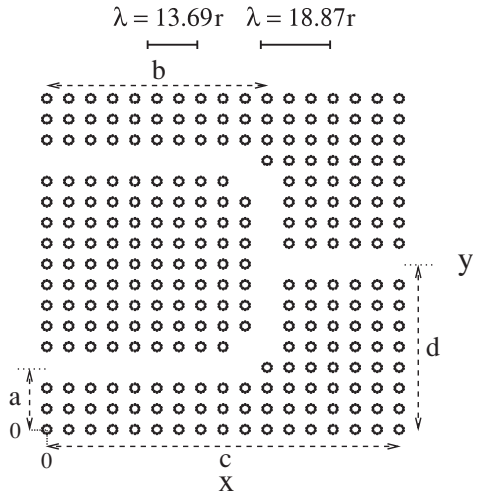

Figure 4. Schematics of a line-defected 'interferometer' waveguide, whose characteristic sizes are $a = 3a_0$, $b = 10a_0$, $c = 16a_0$ and $d = 8a_0$. The indicated wavelengths correspond to $kr = 0.459$ and $kr = 0.333$, respectively.

localized at $x = b$ and $y = a$ (the exact structure is depicted in the inset). We assume an incident plane wave with $kr = 0.4295$, so $\lambda/2$ is approximately equal to the diagonal length

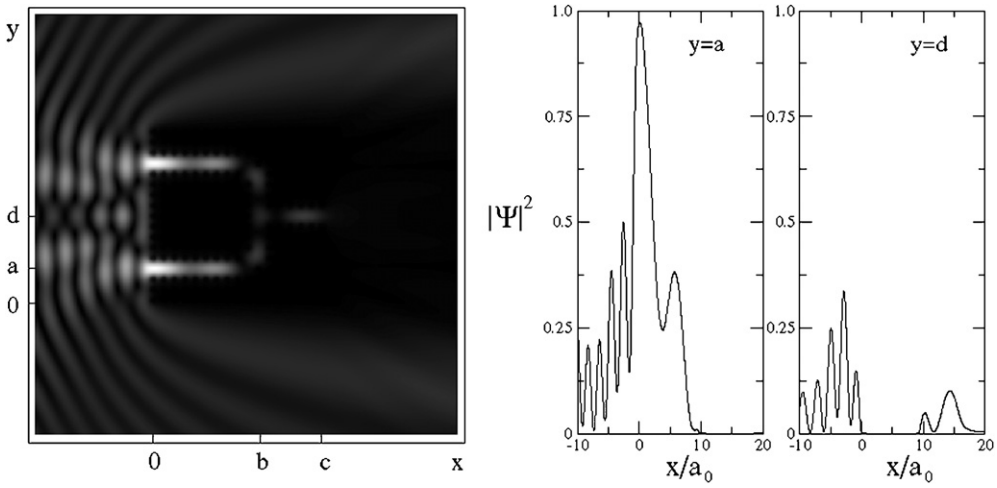

Figure 5. 2D density plot of $|\Psi|^2$ as well as cuts along $y = a$ (lower arm) and $y = d$ (middle arm) for the case of $kr = 0.333$. Although the light beam can penetrate the input channels, the beam bending at the perpendicular line defect is not effective and only a vanishingly small light jet is obtained at the output channel.

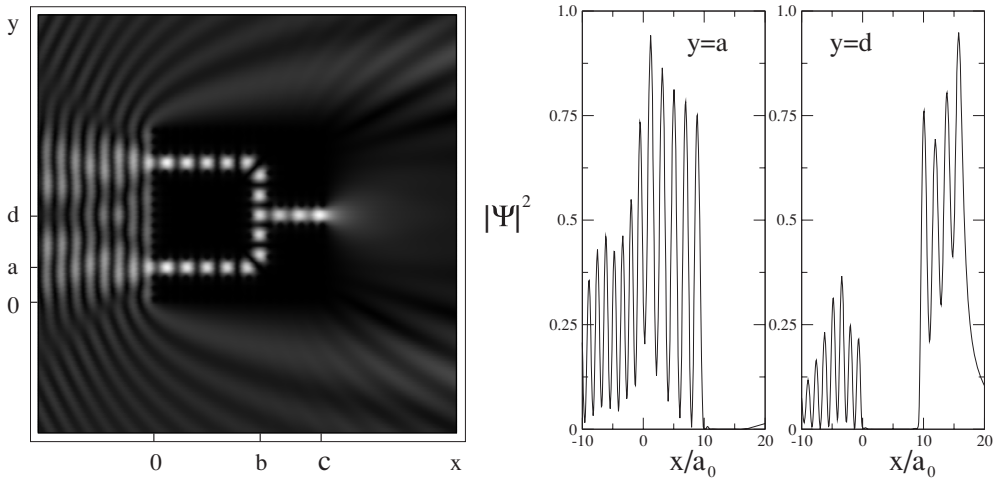

Figure 6. Same as figure 5, but for $kr = 0.459$. In this case, the condition for beam bending is achieved for both the perpendicular and middle line defects. A light jet is obtained at the output channel.

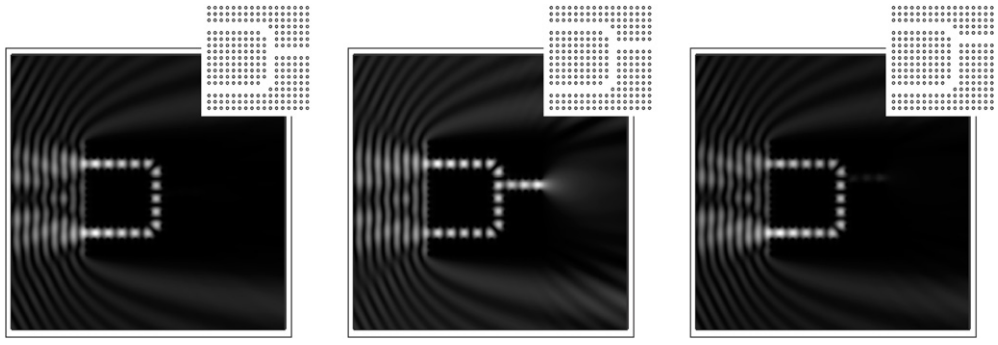

Figure 7. 2D density plots of $|\Psi|^2$ for $kr = 0.459$ and three different spatial configurations for the 'interferometer' waveguide (see the main text). By controlling the difference in the optical path lengths, the condition for constructive interference can be tuned to produce an outgoing light beam.

of the cavity. The system presents a pronounced resonant mode, with an amplitude comparable to that of scattered wave in the external part. This resonance is compatible with a recent estimate, which uses a recursive Green function technique to study the transmission spectrum of a similar photonic structure [15].

Resonance transmission is also expected to take place when two waveguides are coupled by a cavity [1, 15, 24]. Here,

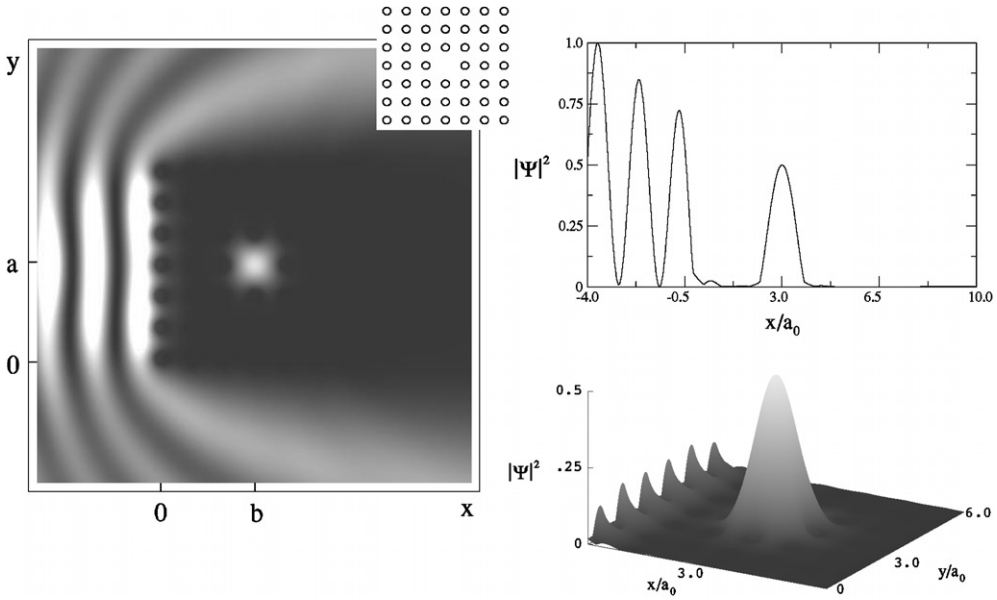

Figure 8. 2D density plot of $|\Psi|^2$, 'cut' along $y = a$, and 3D plot for an incident plane wave with $kr = 0.4295$, for which the cavity has a pronounced resonance. The structure geometry is presented in the inset.

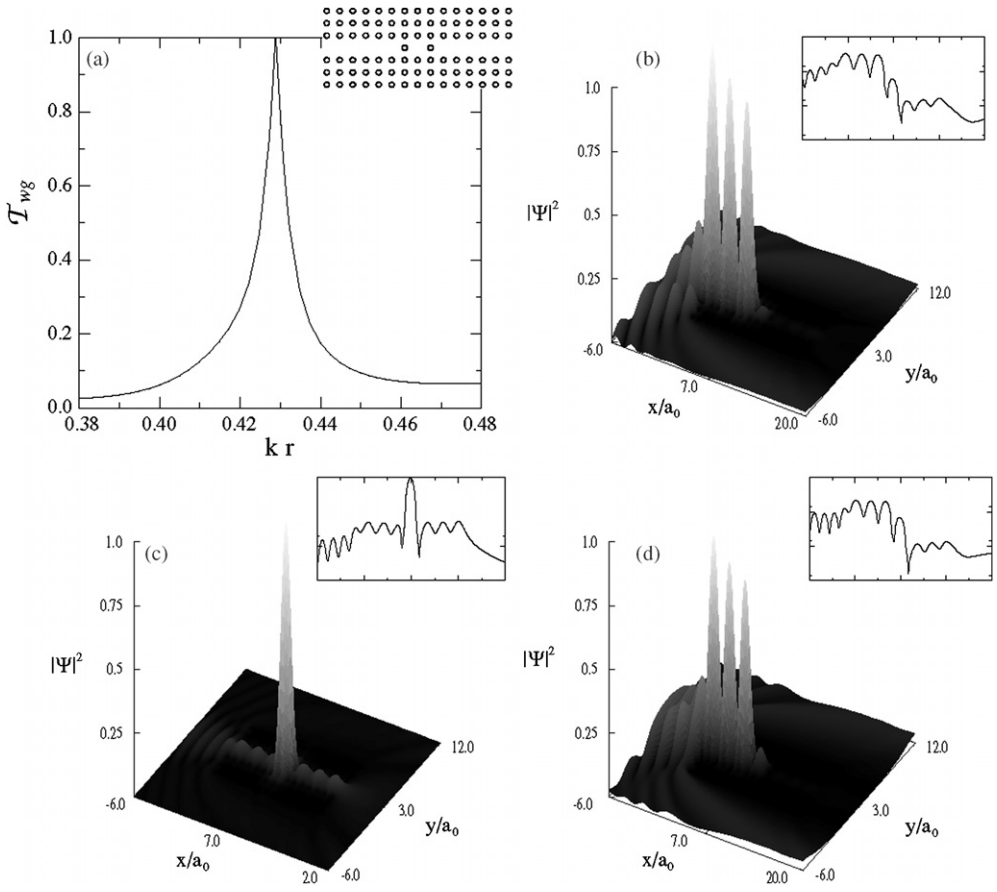

Figure 9. (a) $\mathcal{T}_{wg} \times k$ throughout the structure waveguide shown in the inset. 3D plots of $|\Psi|^2$ for incident plane waves with (b) $kr = 0.42$, (c) $kr = 0.4288$ (the cavity resonance value) and (d) $kr = 0.44$. The insets in the 3D graphs show logarithmic plots for 'cuts' of the $|\Psi|^2$'s along the horizontal centre of the waveguide.

we consider a structure formed by two scatterers separated by an air-type defect. Alternatively, the system can be faced as a waveguide trespassing the whole lattice, but interrupted by a cavity. The geometry is visualized in the inset of figure 9(a). As in the previous case, the cavity has a resonant mode when the half wavelength $\lambda/2$ of the incident wave

is compatible with the cavity's diagonal size. Figure 9(a) shows the transmission $\mathcal{T}_{\rm wg}$ through the waveguide—defined as the ratio of the amplitudes $|\Psi|^2$ of the transmitted wave at the end and beginning of the structure—as a function of the wavenumber k of the incident plane wave. We find that the maximum transmission from the first to the second waveguide is obtained when the incident wave has the same energy of the cavity resonant mode (in the present case corresponding to $kr = 0.4288$). In the density plots of figures 9(b) and (d), the incident waves have values for k lower and greater, respectively, than the resonant mode. Though such k's are close to the resonance value, they still cannot excite the cavity mode and thus only a small transmission to the second waveguide occurs. In figure 9(c), k is under the resonance condition and a mode of large amplitude is formed in the cavity. Also, we see that the wave travelling on the first arm is transmitted to the second. This clearly illustrates the role of the resonant mode in mediating light transport along the waveguides.

5. Remarks and conclusion

In summary, we have demonstrated the potentiality of the boundary wall method to obtain the scattering eigenstates and resonant modes of general 2D photonic band gap nanostructures with typical refraction index contrast. Electromagnetic resonant scattering states localized in the vicinity of line defects were computed with high accuracy using a relatively small computational effort. Besides the beam bending waveguide geometry, we also have explored interferometer-like structures. In this case, the resonant condition for the existence of a localized state within the waveguide has to be combined with the matching condition for the difference between the optical path lengths. Their simultaneous coincidence results in a constructive interference, leading to the emergence of a superposed beam at the waveguide output channel. Finally, for lattices presenting cavities, we have obtained the first resonant mode, which mediates the transmission between waveguides connected by a cavity. The resonance frequencies fall within the visible light and near-infrared spectrum for structures having scattering rods with radius typically in the range of a few tenths of nanometres.

In order to associate the model parameter γ with the transmission coefficient of the photonic crystal structures (see expression (7)), we have assumed the simple case of infinite dielectric interfaces, equation (5). In spite of that, the method was already able to identify the resonance modes in good agreement with those reported by more traditional numerical approaches [15, 22]. Obviously, whenever such an assumption may become an issue, one should consider a more appropriate expression for $\mathcal{T}_{\rm EM}$ so as to identify it with $\mathcal{T}$ in equation (6).

Due to the simplicity of the numerical procedure, much more complex structures can be explored in the search for optimal geometries and parameter values needed to perform a predetermined task. In fact, this is the great advantage of the BWM over other techniques. The freedom of choice and variation of scatterer parameters makes the BWM a good approach to finding scattering and resonant states in both known and new structures. Recently, this method has been applied to the study of an organic photodetector device with a metal nano-indented mask for light harvesting. The optimal parameters for the device were first obtained by BWM simulations and then used in the experimental implementation, with a considerable efficiency gain [25].

Considering the above comments, we mention two contexts where the BWM can be particularly useful. The first is the study of branching networks (circuits), fabricated by tailoring appropriate defect lines along the photonic crystal structure [26]. The resulting net of connected waveguides will present a great variety of interference effects, leading to a complex dynamics for light transport. The BWM is quite amenable to deal with this type of design, as already seen in section 3 in the simpler example of an interferometer-like device. The second is to understand how imperfections in photonic crystals, e.g., due to some structural disorder or surface roughness, can give rise to scattering losses [1, 20, 27], eventually rendering impossible certain applications. For instance, even small dislocations of a single rod at the corner of a $\pi/2$ waveguide may destroy resonant transmission. Although efficient approaches to quantifying such phenomena do exist [20, 27], some can be a little cumbersome to carry out and better suited to simulating average disorder, instead of localized imperfections. Since changes in the position and properties of individual rods in a photonic crystal structure are easy to implement with the BWM, it becomes very appropriate to address this problem.

Potentially, the method can also be used to obtain the scattering states of photonic crystal slabs [28], photonic band-gap fiberes [29] and general 3D photonic crystal structures [30]. However, the light polarization has to be taken into account carefully in these cases. It would be interesting to see also the BWM extended to the study of nonlinear optical phenomena in photonic band-gap crystals [31]. We hope that the present work will motivate further applications of the boundary wall method in this rapidly developing area.

Acknowledgments

The authors gratefully acknowledge CNPq and CAPES for research fellowships. Financial support is also provided by CT-Infra, CT-Energ, CNPq-Edital Universal, PRONEX, Fundação Araucária and FAPEAL.

Appendix. A simple numerical implementation for the BWM

Here we present just the main steps towards numerically implementing the BWM. A detailed discussion, including convergence criterium, ways to speed up the protocol, comparison with other methods, how to handle the case of $\gamma \to \infty$, etc, can be found in [11].

We start by considering an arbitrary border $\mathcal{C}$ and dividing it into N segments, so to form the set $\{\mathcal{C}_j\}$, $j = 1, 2, \ldots, N$. In this way, equation (1) reads (with γ being assumed constant and dropping the notation for the k dependence)

$$\Psi(\mathbf{r}) = \varphi(\mathbf{r}) + \sum_{j=1}^{N} \gamma \int_{\mathcal{C}_j} \mathrm{d}s\, G_0(\mathbf{r}, \mathbf{r}(s))\Psi(\mathbf{r}(s)). \tag{A.1}$$

If we now suppose s_j a point on $\mathcal{C}_j$ (in practice, usually taken as its middle) and if the segments are made very small, the above equation can be approximated by

$$\begin{aligned}\Psi(\mathbf{r}) &\approx \varphi(\mathbf{r}) + \sum_{j=1}^{N} \gamma \int_{\mathcal{C}_j} \mathrm{d}s\, G_0(\mathbf{r}, \mathbf{r}(s))\Psi(\mathbf{r}(s_j)) \\ &\approx \varphi(\mathbf{r}) + \sum_{j=1}^{N} \gamma \Psi(\mathbf{r}(s_j)) \int_{\mathcal{C}_j} \mathrm{d}s\, G_0(\mathbf{r}, \mathbf{r}(s)).\end{aligned} \tag{A.2}$$

Next, by setting $\mathbf{r} = \mathbf{r}_i$, with s_i a point of $\mathcal{C}_i$, we get

$$\begin{aligned}\Psi(\mathbf{r}_i) &\approx \varphi(\mathbf{r}_i) + \sum_{j=1}^{N} \mathbb{M}_{ij}\gamma\Psi(\mathbf{r}_j), \\ \mathbb{M}_{ij} &\equiv \int_{\mathcal{C}_j} \mathrm{d}s G_0(\mathbf{r}_i, \mathbf{r}(s)).\end{aligned} \tag{A.3}$$

Analogously to the above procedure, from the definition in equation (2) we can write $\Psi(\mathbf{r}_i) \approx \sum_j \mathbb{T}_{ij}\varphi(\mathbf{r}_j)$, which defines a discretized version ($\mathbb{T}$) of T. Then, by a direct comparison between such an expression and equation (A.3), we have

$$\mathbb{T} = \gamma[\mathbb{I} - \gamma\mathbb{M}]^{-1}. \tag{A.4}$$

Finally, for $\int_{\mathcal{C}_j} \mathrm{d}s G_0(\mathbf{r}, \mathbf{r}(s)) \approx G_0(\mathbf{r}, \mathbf{r}_j)\Delta_j$ (with Δ_j the length of $\mathcal{C}_j$), $\Phi = (\varphi(\mathbf{r}_1), \ldots, \varphi(\mathbf{r}_N))^{\mathrm{T}}$, and using the discrete version of T in (A.4), we find for equation (A.2)

$$\Psi(\mathbf{r}) \approx \varphi(\mathbf{r}) + \sum_{j=1}^{N} G_0(\mathbf{r}, \mathbf{r}_j)\Delta_j(\mathbb{T}\Phi)_j. \tag{A.5}$$

Regarding the expression for $\mathbb{M}$, equation (A.3), if $i \neq j$ we can write $\mathbb{M}_{ij} \approx G_0(\mathbf{r}_i, \mathbf{r}_j)\Delta_j$. For $i = j$, $G_0(\mathbf{r}_i, \mathbf{r}_i)$ diverges due to its logarithmic behaviour for small argument values (recall that in 2D, G_0 is given in terms of the zero-order Hankel function of first kind). Hence, $\mathbb{M}_{ii}$'s must be calculated directly from the integral in equation (A.3). Fortunately, it can always be performed analytically from appropriate series expansions for G_0, since it holds that for $|z|$ small $H_0(z) \approx 1 - (z/2)^2 + (2i/\pi)(\ln[z/2] + \Gamma) + \cdots$, with Γ the Euler constant. This is what we have done in all our numerical examples.

References

[1] Johnson S G and Joannopoulos J D 2002 *Photonic Crystals: the Road from Theory to Practice* (Boston, MA: Kluwer)
[2] Johnson S G and Joannopoulos J D 2003 *Acta Materiallia* **51** 5823
[3] Joannopoulos J D, Villeneuve P R and Fan S H 1997 *Nature* **386** 143
[4] Yablonovitch E 1993 *J. Phys.: Condens. Matter* **5** 2443
[5] Yablonovitch E 1987 *Phys. Rev. Lett.* **58** 2059
[6] Edelstein A S 2003 *J. Magn. Magn. Mater.* **256** 430
[7] da Luz M G E, Lupu-Sax A S and Heller E J 1997 *Phys. Rev.* E **56** 2496
[8] Li L M and Zhang Z Q 1998 *Phys. Rev.* B **58** 9587
[9] Katine J A, Eriksson M A, Adourian A S, Westervelt R M, Edwards J D, Lupu-Sax A S, Heller E J, Campman K L and Gossard A C 1997 *Phys. Rev. Lett.* **79** 4806
[10] Vaishnav J Y, Itsara A and Heller E J 2006 *Phys. Rev.* B **73** 115331
Vaishnav J Y, Walls J D, Apratim M and Heller E J 2007 *Phys. Rev.* A **76** 013620
[11] Zanetti F M, Vicentini E and da Luz M G E 2008 *Ann. Phys.* NY **323** 1644
[12] Paddon P and Young J F 2000 *Phys. Rev.* B **61** 2090
Asatryan A A, Busch K, McPhedran R C, Botten L C, de Sterke C M and Nicorovici N A 2001 *Phys. Rev.* E **63** 046612
Cheng H, Crutchfield W Y, Doery M and Greengard L 2004 *Opt. Express* **12** 3791
Zhao L-M, Wang X-H, Gu B-Y and Yang G-Z 2005 *Phys. Rev.* E **72** 026614
[13] Yang W and Gopinath A 1995 *Photonics Tech. Lett.* **7** 777
Paulus M and Martin O J F 2001 *Phys. Rev.* E **63** 066615
Haider M A, Shipman S P and Venakieds S 2002 *SIAM J. Appl. Math.* **62** 2129
Habu S, Takenaga K, Himeno K and Wada A 2003 *J. Lightwave Tech.* **21** 1787
Shipman S P and Venakides S 2005 *Phys. Rev.* E **71** 026661
Cho M H, Cai W and Her T-H 2006 *J. Sci. Comp.* **28** 263
[14] Leung K M and Qiu Y 1993 *Phys. Rev.* B **48** 7767
[15] Rahachou A I and Zozoulenko I V 2005 *Phys. Rev.* B **72** 155117
[16] Hammer M 2004 *Opt. Commun.* **235** 285
[17] Joannopoulos J D, Villeneuve P R and Fan S 1997 *Solid. State Commun.* **102** 165
[18] Vodo P, Parimi P V, Lu W T, Sridhar S and Wing R 2004 *Appl. Phys. Lett.* **85** 1858
Li J, Sun G and Chan C T 2006 *Phys. Rev.* B **73** 075117
[19] Parimi P V, Lu W T, Vodo P, Sokoloff J, Derov J S and Sridhar S 2004 *Phys. Rev. Lett.* **92** 127401
[20] Frei W R and Johnson H T 2004 *Phys. Rev.* B **70** 165116
[21] Miroshnichenko A E and Kivshar Y S 2005 *Opt. Express* **13** 3969
[22] Mekis A, Chen J C, Kurland I, Fan S, Villeneuve P R and Joannopoulos J D 1996 *Phys. Rev. Lett.* **77** 3787
[23] Martinez A, Sanchis P and Marti J 2005 *Opt. Quantum Electron.* **37** 77
[24] Li Z-Y and Ho K-M 2003 *Phys. Rev.* B **68** 155101
[25] Macedo A G, Zanetti F M, Mikowski A, Hummelen J C, Lepienski C M, da Luz M G E and Roman L S 2008 *J. Appl. Phys.* **104** 033714
[26] Kuchment P and Kunyansky L A 1999 *Exp. Math.* **8** 1
McGurn A R 2000 *Phys. Rev.* B **61** 13235
[27] Langtry T, Botten L, Asatryan A and McPhedran R 2003 *Math. Comp. Simul.* **62** 385
Hughes S, Ramunno L, Young J F and Sipe J E 2005 *Phys. Rev. Lett.* **94** 033903
[28] Johnson S G, Fan S H, Villeneuve P R, Joannopoulos J D and Kolodziejski L A 1999 *Phys. Rev.* B **60** 5751
[29] Ouzounov D G, Ahmad F R, Muller D, Venkataraman N, Gallagher M T, Thomas M G, Silcox J, Koch K W and Gaeta A L 2003 *Science* **301** 1702
[30] Li Z-Y and Xia Y 2001 *Phys. Rev.* A **63** 043817
[31] Berger V 1998 *Phys. Rev. Lett.* **81** 4136